ANALYSIS OF EXCAVATION-INDUCED DEFORMATION WITH DIFFERENT SOIL MODELS

MARCIN CUDNY[1] AND PAWEŁ POPIELSKI[2]

[1]*Department of Geotechnics, Geology and Maritime Engineering,*
Faculty of Civil and Environmental Engineering,
Gdansk University of Technology,
Narutowicza 11/12, 80-233 Gdansk, Poland
mcud@pg.gda.pl

[2]*Hydro-Engineering and Hydraulic Department,*
Faculty of Environmental Engineering,
Warsaw University of Technology,
Nowowiejska 20, 00-653 Warsaw, Poland

Abstract: The monitored case of deep excavation works located in the centre of Warsaw is described and back analysed as a boundary value problem with the finite element method. The excavation was carried out in over-consolidated clayey layers under the support of braced diaphragm walls. Accurate simulation of such soil-structure interaction problems requires advanced soil constitutive models – especially for the pre-failure range of small strains. On the other hand, such models should not be very complex and their material parameters should be relatively simple to obtain from laboratory and *in situ* surveys. By means of a case study, this paper examines several simple elasto-plastic constitutive models for the simulation of the behaviour of soil layers. The influence of such characteristics of the soil behaviour, as anisotropy and non-linearity of stiffness, is studied in the paper. The discussion concerns the problems related to the application of the models for a practical example. The comparison is focused on the obtained and measured displacements of the neighbouring building and diaphragm walls.

Keywords: deep excavation, constitutive modelling, ground deformation, finite element method, case histories

1. Introduction

Construction activities, particularly those related to the improvement of the infrastructure in densely populated city areas, often take place in close vicinity of existing buildings. One of the most problematic engineering operations in such a situation is the execution of deep excavations. Changes in the stress state in the

ground, which occur during the excavation, cause deformations of the surrounding soil layers and displacements of the foundations of existing structures. This may be dangerous, especially for tall buildings or old, historical structures. The correct estimation of these displacements, as well as a safe design of the excavation support, become a crucial task for geotechnical engineers.

Nowadays, a given deep excavation case is often treated as a boundary value problem and solved numerically with the finite element method. The most important aspects in such numerical analysis are the choice of an appropriate constitutive model for the description of soil behaviour, and the estimation of material parameters. An excavation is an instance of unloading of the ground, and in the event of a properly designed support, the soil surrounding the excavation area undergoes relatively small strains. In this situation, the stiffness of the soil is high and the standard design secant stiffness moduli of soil, which are commonly used in the Mohr-Coulomb model, are generally inadequate for numerical calculations. The soil stiffness has a direct influence on the behaviour of an applied support system and its structural strength. The accurate simulation of this soil-structure interaction problem requires advanced soil constitutive models – especially for the range of small and intermediate strains ($\leq 10^{-3}$). However, such models should not be overly complicated and their material parameters have to be relatively simple to obtain from laboratory and *in situ* surveys. It should also be clear how to set the initial values of state variables in the model and how to set the initial stress conditions.

By means of a case study, this paper examines several constitutive models for the simulation of the behaviour of soil layers. The soil models are formulated within a simple elasto-plastic framework. The shear strength criterion of Matsuoka-Nakai [1] is used with different formulations of the stiffness characteristics inside the yield locus. The following stiffness formulations are examined: linear isotropic elastic, anisotropic linear elastic, and non-linear hyperelastic and para-elastic.

2. Analysed case of deep excavation

The analysed excavation pit is located in the centre of Warsaw. It was designed for a two-storey underground garage underneath a multi-storey building. The top-down method was applied with a single floor slab at the depth of 1.8 m below the ground level. The final depth of the excavation was 10.2 m. Diaphragm walls 14.2 m long and 0.8 m thick were used to support the excavation. The plan view of the excavation is shown in Figure 1. Geometry, loading details and finite element discretisation of the analysed plane strain section of the excavation is presented in Figure 2. Loading details are presented for the closing stage of the underground part of the structure, without additional loadings from the new building. A nine-storey bank building, founded on a slab at the depth of 5 m below the ground level, is located in the neighbourhood of the excavation pit. In the analysed section, the distance between the bank building and the

excavation is 10.8 m. The lower part of the diaphragm walls ends 3.4 m within the low permeability sandy clay. This allowed carrying out the earthworks without lowering the existing water level. Dewatering was carried out only at the bottom of the excavation pit.
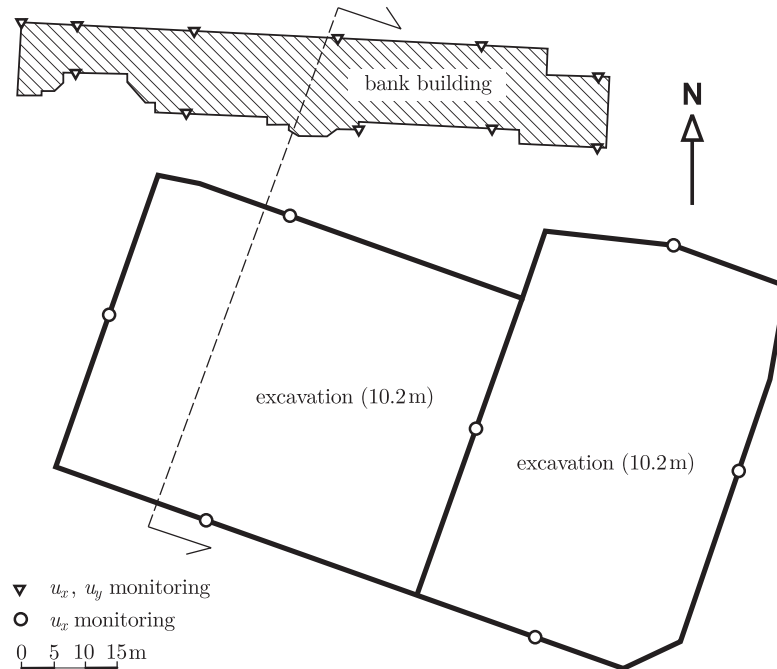

Figure 1. Plan view of the excavation and measurement instrumentation with the location of the 2D section used in the plane strain calculations

The vertical (u_x) and horizontal (u_y) displacements of the foundations of the neighbouring bank building, as well as the horizontal movement of the diaphragm walls (u_x), were monitored by geodetic survey. The location of the benchmarks is shown in Figure 1.

2.1. Soil layers and water conditions

Soil layers with basic material properties and water conditions are shown in Figure 3. From the geomorphological point of view, the terrain is formed by the denudation of the glacial upland. It represents the so-called Warsaw level of the Vistula River Valley.

The characteristic soil layers are distinguished for the purposes of analysis, based on the results of drilling, cone penetration and supplementary dilatometric tests (Barański *et al.* [2]). In the model, the layers are assumed to be parallel and horizontal, which is a simplification. However, the deviations observed due to this idealisation are not significant in the analysed section. The first soil layer is a heterogeneous silty fill with some content of rubble and humus. The subsequent layer 2 includes sandy deposits related to the denudation processes of the North
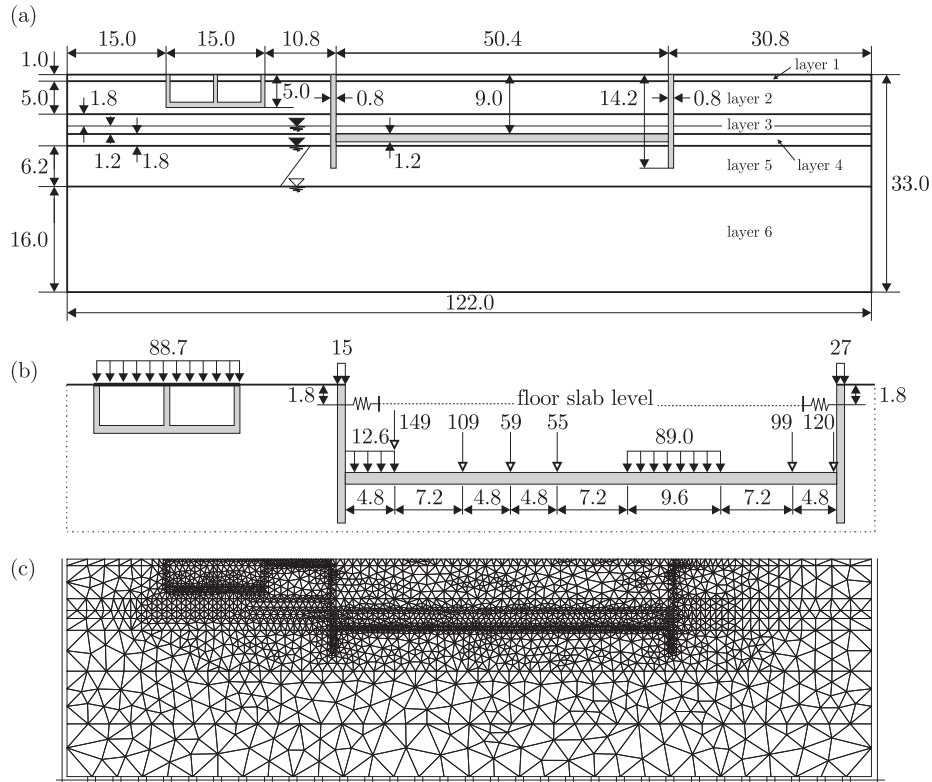
Figure 2. Geometry and finite element mesh used in the calculations: (a) – soil layers and dimensions of the problem; (b) – loading details, distributed loading [kPa], line loadings [kN/m]; (c) – full finite element mesh used for the initiation of the *in situ* stress (6-node quadratic pore pressure elements are used)

Polish Glaciation and the fluvioglacial formations of the Wartanian Glaciation, which belong to the Middle Polish Glaciations. These soils are of medium density and stiffness. Layer 3 represents the stagnation clayey deposits of medium stiffness. The formations of layers 4 and 5 are related to the Odranian Glaciation – the older Middle Polish Glaciation. The fluvioglacial medium dense sands of layer 4 are deposited over the continuous and thick layer 5, composed of high stiffness clay. Deeper deposits correspond to the Great Interglacial and are represented by dense sands (layer 6). The thickness of this layer exceeds 10m and was not estimated by drilling. In the model, this layer is chosen as a bottom layer, which limits the boundary problem. All natural layers in the analysed profile are over-consolidated with $OCR > 10$.

The first unconfined aquifer is built of the sand layer 4 and partly of layer 3. The water level of this aquifer changes seasonally. The second aquifer is built of the bottom sand layer 6 and is confined by the low permeability clay layer 5. The hydraulic head in this aquifer corresponds to the level located between layers 4 and 5.
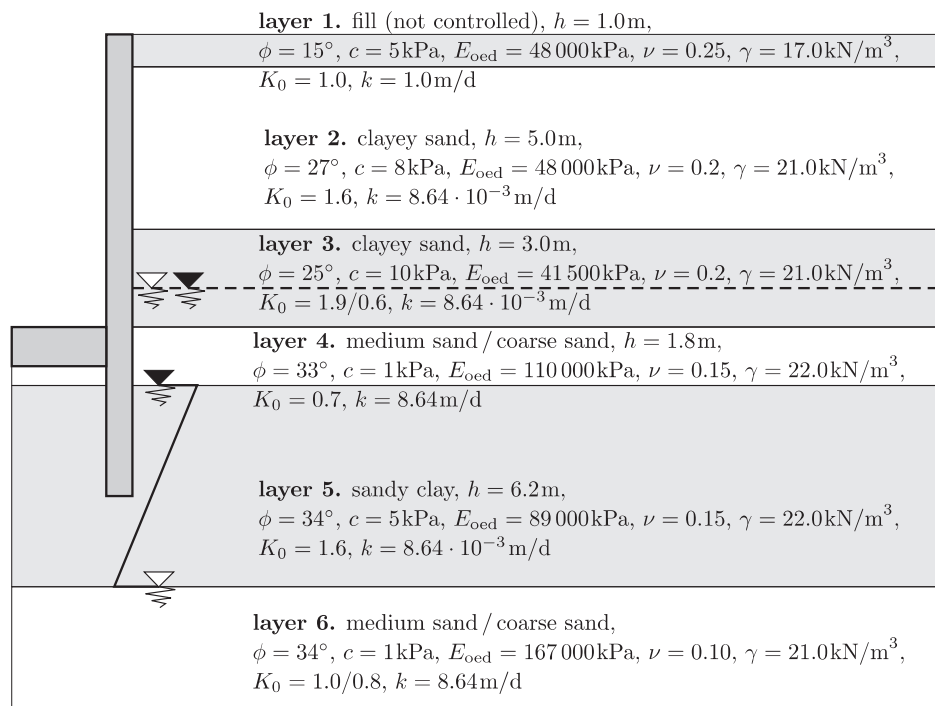
layer 1. fill (not controlled), $h = 1.0$m,
$\phi = 15°$, $c = 5$kPa, $E_{\text{oed}} = 48\,000$kPa, $\nu = 0.25$, $\gamma = 17.0$kN/m^3,
$K_0 = 1.0$, $k = 1.0$m/d

layer 2. clayey sand, $h = 5.0$m,
$\phi = 27°$, $c = 8$kPa, $E_{\text{oed}} = 48\,000$kPa, $\nu = 0.2$, $\gamma = 21.0$kN/m^3,
$K_0 = 1.6$, $k = 8.64 \cdot 10^{-3}$m/d

layer 3. clayey sand, $h = 3.0$m,
$\phi = 25°$, $c = 10$kPa, $E_{\text{oed}} = 41\,500$kPa, $\nu = 0.2$, $\gamma = 21.0$kN/m^3,
$K_0 = 1.9/0.6$, $k = 8.64 \cdot 10^{-3}$m/d

layer 4. medium sand / coarse sand, $h = 1.8$m,
$\phi = 33°$, $c = 1$kPa, $E_{\text{oed}} = 110\,000$kPa, $\nu = 0.15$, $\gamma = 22.0$kN/m^3,
$K_0 = 0.7$, $k = 8.64$m/d

layer 5. sandy clay, $h = 6.2$m,
$\phi = 34°$, $c = 5$kPa, $E_{\text{oed}} = 89\,000$kPa, $\nu = 0.15$, $\gamma = 22.0$kN/m^3,
$K_0 = 1.6$, $k = 8.64 \cdot 10^{-3}$m/d

layer 6. medium sand / coarse sand,
$\phi = 34°$, $c = 1$kPa, $E_{\text{oed}} = 167\,000$kPa, $\nu = 0.10$, $\gamma = 21.0$kN/m^3,
$K_0 = 1.0/0.8$, $k = 8.64$m/d

Figure 3. Soil layers, water conditions and the basic material parameters

The Continuous Surface Wave System (CSWS) geophysical technique was used for evaluating the small strain stiffness of soil layers (Matthews *et al.* [3]). The CSWS survey results are presented in Figure 4, where we present the average changes of the small strain Young's modulus with depth, as well as operational moduli used in the calculations.

3. Constitutive models

The soil layers in the analysed problem are the over-consolidated clayey deposits with dense, granular, saturated soils at the bottom of the analysed area. Field observations from similar excavations in the vicinity demonstrate that the ground is very stiff, with high bearing capacity, and typically, during the period of excavation works a heave of the surrounding terrain was observed. This suggests that the soils mostly undergo unloading or reloading within the so-called small and intermediate strain regions. However, in the vicinity of diaphragm walls, larger plastic shear strains may develop locally. Taking this as an assumption, the constitutive model of soil may be simplified for practical aims. Here, the elastic – rigid plastic framework is employed with the focus on the modelling of the pre-failure behaviour of natural soils. The yield locus is formulated only by the shear strength criterion, without introducing the cap surface and volumetric hardening, which is irrelevant/inconsequential in the analysis of soil behaviour in the case of high over-consolidation.
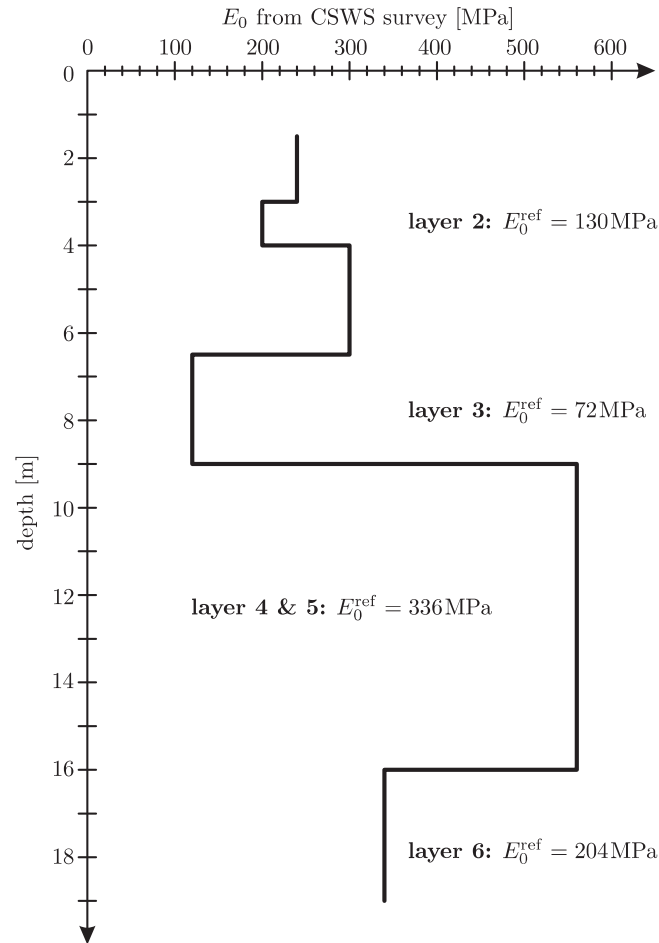
Figure 4. Small strain stiffness Young's moduli from the CSWS survey. Shear moduli G_0 in the para-elastic model are calculated from the operational values E_0^{ref}

3.1. Matsuoka-Nakai base model

Basic soil parameters used in routine calculations concern the Mohr-Coulomb model, which is always implemented in the geotechnically-oriented finite element programs. The Mohr-Coulomb model realises the elastic-rigid plastic constitutive law, which is based on the Hooke's isotropic linear elasticity and Mohr-Coulomb shear criterion for the yield function and plastic potential. The strength parameters are: ϕ, c, ψ – the effective friction angle, effective cohesion and dilatancy angle, respectively. The stiffness parameters are chosen differently, according to local practice (*e.g.* Poisson's ratio ν and the oedometer modulus E_{oed} or Young's modulus E). The elastic stiffness may be expressed in the following form:

$$D_{ijkl}^e = \frac{E}{(1+\nu)(1-2\nu)}\left[\nu\delta_{ij}\delta_{kl} + \frac{1-2\nu}{2}(\delta_{ik}\delta_{jl} + \delta_{jk}\delta_{il})\right] \tag{1}$$

Although it is unclear what kind of stiffness parameters need to be used, this model is very often applied in practical calculations. In most cases, the secant stiffness moduli from standard triaxial or oedometer tests are employed and the Poisson's ratio is chosen arbitrarily, according to experience. However, this method is very imprecise if an accurate estimation of displacements and of the soil responses under the small strain conditions is expected, as in the case of well-designed strutted deep excavation works.

The Mohr-Coulomb yield contour on the deviatoric plane represents the isoline of the constant friction angle. It is a conservative approach, which according to experimental evidence underestimates the shear strength for the plane strain conditions (Eekelen [4]). In the present study, the set of Mohr-Coulomb model parameters is retained, however, a different yield function is chosen to represent the shear strength for non-axisymmetric stress conditions more realistically.

Among smooth yield surfaces reported in the literature, the shear criterion of Matsuoka and Nakai, based on the so-called *spatially mobilised plane* concept is adopted [1]. This criterion agrees with the Mohr-Coulomb model for axisymmetric compression and extension, and allows slightly higher shear strengths for non-axisymmetric stress states. The shear strength criterion is defined as:

$$f = -\frac{I_1}{I_2 I_3} + \frac{9 - \sin^2\phi}{-1 + \sin^2\phi} = 0 \tag{2}$$

where I_1, I_2, I_3 are the stress invariants:

$$I_1 = \sigma_{kk} \tag{3}$$

$$I_2 = \frac{1}{2}\left[\sigma_{ij}\sigma_{ij} - (I_1)^2\right] \tag{4}$$

$$I_3 = \det(\boldsymbol{\sigma}) \tag{5}$$

If cohesion needs to be included, the invariants are calculated for the modified stress state $\sigma_{ij}^* = \sigma_{ij} - p_c\delta_{ij}$, where $p_c = c\cot\phi$.

The Drucker-Prager function is taken as the plastic potential and is defined as:

$$g = q - \frac{6\sin\psi}{3 - \sin\psi}p \tag{6}$$

where ψ is the dilatancy angle and p, q are mean and deviatoric stress invariants, respectively:

$$p = -\frac{1}{3}\sigma_{kk}, \quad q = \sqrt{\frac{3}{2}s_{ij}s_{ij}} \tag{7}$$

$\boldsymbol{s}$ is the deviatoric part of the stress tensor $(s_{ij} = \sigma_{ij} + p\delta_{ij})$.

The use of the Drucker-Prager function, instead of the Matsuoka-Nakai function for the plastic potential, is again a simplification which helps in the implementation of the model (owing to its simple definition and stress derivatives). This simplification is based on the fact that the actual values of the dilatancy angle for soils are small ($\leq 10°$). From this it ensues that the isolines of both functions on the deviatoric and meridian planes in the principal stress space are very similar and overlap for $\psi = 0°$.

In the following sections, we will build on the simple elasto-plastic model of Matsuoka-Nakai by modifying the stiffness formulation (1).

All presented models are implemented into the displacement-based commercial finite element code PLAXIS within the user-defined soil models facility (Brinkgreve *et al.* [5]). The backward Euler return algorithm is used for the local integration of constitutive relations. To this end, the Newton-Raphson iterative procedure is used, as described by Jeremić and Sture [6].

3.2. Linear anisotropic stiffness

Directional dependence of mechanical properties prevails in natural soils. Deposition, diagenesis and consolidation of pre-glacial, as well as post-glacial, soil deposits produce a microstructure with a preferred particle orientation. This directly influences the stiffness and strength anisotropy. The degree of strength anisotropy may be changed during the monotonic loading process, however, the small strain stiffness anisotropy remains, even after significant straining, which may be demonstrated by stress probe testing after unloading (Jovičić and Coop [7]). The importance of taking the anisotropic stiffness characteristics into account has already been demonstrated by many authors for some practical cases, *e.g.* Poulos [8], Simpson *et al.* [9], Addenbrooke *et al.* [10] or Kung *et al.* [11].

The deposition and strain history in most of the soils are essentially one-dimensional with a single vertical axis of symmetry. This common type of anisotropy is known as cross-anisotropy or transverse isotropy. A full description of cross-anisotropic elasticity requires five independent constants. They are usually chosen as follows: Young's modulus in the vertical direction, E_v; Young's modulus in the horizontal direction, E_h; Poisson's ratio for horizontal strain due to vertical strain, ν_{vh}; Poisson's ratio for horizontal strain due to horizontal strain at right angles, ν_{hh}; shear modulus in the vertical plane, G_{hv}. Because of the thermodynamic requirement of positive strain energy which holds in the elastic material, there are bounds for the values of parameters of cross-anisotropy. For details, the reader is referred to Pickering [12].

In routine calculations, all five parameters of cross-anisotropy are usually not available. From the standard triaxial test, equipped with accurate transducers for the measurements of both vertical and horizontal displacements, the parameters E_v and ν_{vh} may be estimated. Obtaining the remaining parameters for the cross-anisotropy requires more advanced testing procedures (Lings *et al.* [13]). An alternative, three-parameter formulation of cross-anisotropy was proposed by Graham and Houlsby [14]. This model represents a limited form of cross-anisotropy and involves only one parameter in addition to the two that are required to describe an isotropic elastic material. The material constants of the three-parameter Graham-Houlsby model are: modified Young's modulus, E^*; modified Poisson's ratio, ν^*; the anisotropy factor, α. The factor α simply fixes the ratio of Young's modulus, Poisson's ratio and shear modulus in the following way:

$$\alpha = \sqrt{\frac{E_h}{E_v}} = \frac{\nu_{hh}}{\nu_{vh}} = \frac{G_{hh}}{G_{hv}} \tag{8}$$

where G_{hh} is the shear modulus in the horizontal plane, which is related to the parameters of cross-anisotropy by the expression:

$$G_{hh} = \frac{E_h}{2(1+\nu_{hh})} \tag{9}$$

A comparison between all five parameters of cross-anisotropy and the three parameters of the Graham-Houlsby model leads to:

$$E_v = E^* \tag{10}$$

$$E_h = \alpha^2 E^* \tag{11}$$

$$\nu_{vh} = \frac{\nu^*}{\alpha} \tag{12}$$

$$\nu_{hh} = \nu^* \tag{13}$$

$$G_{hv} = \alpha \frac{E^*}{2(1+\nu^*)} \tag{14}$$

The stiffness of the Graham-Houlsby cross-anisotropic model in the simplified form of a 6×6 matrix in the principal directions of anisotropy may be expressed within the stress-strain relation as:

$$\begin{Bmatrix} \dot\sigma_{11} \\ \dot\sigma_{22} \\ \dot\sigma_{33} \\ \dot\sigma_{12} \\ \dot\sigma_{23} \\ \dot\sigma_{31} \end{Bmatrix} = \frac{E^*}{(1+\nu^*)(1-2\nu^*)} \begin{bmatrix} A & C & D & 0 & 0 & 0 \\ C & B & C & 0 & 0 & 0 \\ D & C & A & 0 & 0 & 0 \\ 0 & 0 & 0 & E & 0 & 0 \\ 0 & 0 & 0 & 0 & E & 0 \\ 0 & 0 & 0 & 0 & 0 & F \end{bmatrix} \begin{Bmatrix} \dot\varepsilon_{11} \\ \dot\varepsilon_{22} \\ \dot\varepsilon_{33} \\ \dot\varepsilon_{12} \\ \dot\varepsilon_{23} \\ \dot\varepsilon_{31} \end{Bmatrix} \tag{15}$$

where

$$A = \alpha^2(1-\nu^*) \tag{16}$$

$$B = 1-\nu^* \tag{17}$$

$$C = \alpha\nu^* \tag{18}$$

$$D = \alpha^2\nu^* \tag{19}$$

$$E = \alpha(1-2\nu^*) \tag{20}$$

$$F = \alpha^2(1-2\nu^*) \tag{21}$$

Note that, unusually, the stress components σ_{ij} and the strain components ε_{ij} are written in the vector form and directions x_1 and x_3 are the horizontal directions and x_2 is the vertical direction. This is the order used in the applied finite element code, however, this needs to be examined, and perhaps reorganised, when implementing the model in other computer programs.

A comparison of different stiffness formulations may be obtained by confronting the so-called response envelopes. The response envelopes are polar diagrams of stiffness drawn for visualisation purposes (Gudehus [15]). They are usually shown in the triaxial stress plane as closed curves, showing response to
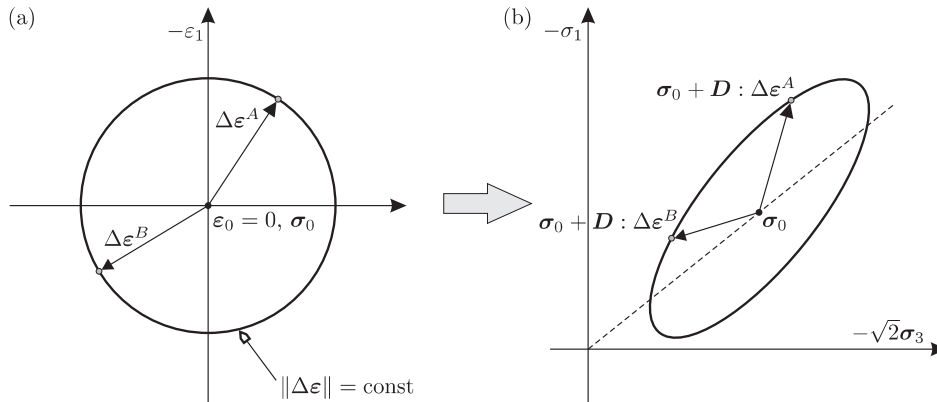
Figure 5. Response envelope in the triaxial plane in the principal stress space – a polar diagram of stiffness $\boldsymbol{D}$; (a) – input circular strain probe; (b) – output stress response envelope

the circular strain probe. The schematic description for obtaining the response envelopes is presented in Figure 5.

The influence of the factor α on the shape and rotation of the response envelopes for the cross-anisotropic elasticity is presented in Figure 6. Taking the value $\alpha = 1.0$ gives the isotropic Hooke's elasticity. The response envelopes for isotropic elasticity are elliptical curves, which are oriented parallel to the hydrostatic axis ($\sigma_1 = \sigma_2 = \sigma_3$). The shape is controlled by the Poisson's ratio and the size is proportional to the value of Young's modulus. Using a value of α other than 1.0 results in a rotation of the main axes of the response envelope. For $\alpha > 1.0$, the rotation is clockwise and for $\alpha < 1.0$, it is anticlockwise. A similarity can be observed with the shape of yield surfaces for natural, over-consolidated and normally consolidated clayey soils, respectively. However, fixing the value of the vertical Young's modulus E_v, while rotating the response envelope results in a significant change of its size. This signifies an important change of the stiffness for the radial stress path directions other than the triaxial compression ($\Delta\sigma_1 \neq 0, \Delta\sigma_2 = \Delta\sigma_3 = 0$). Generally, for $\alpha > 1.0$, the response envelope is stretched and for $\alpha < 1.0$, it is compressed when compared with the isotropic case ($\alpha = 1.0$). If the size of the isotropic response envelope needs to be retained, then the value of $E_v = E^*$ also needs to be adjusted. However, the application of different values of α slightly influences the proportions of the response envelopes.

3.3. Non-linear hyperelastic stiffness

Another important feature of the soil stiffness is its stress dependency. Some empirical relations for stress dependency of the stiffness moduli are well known in the literature (*e.g.* Ohde [16], Janbu [17], Houlsby and Wroth [18]) and are used to formulate general stress-strain relations. Usually, in the Equation (1) the value of Poisson's ratio is kept constant and the preferred empirical relation $E = E(\boldsymbol{\sigma})$ is introduced. However, this results in hypoelastic stiffness, which may render unrealistic behaviour for some closed unloading-reloading loops (Zytynski
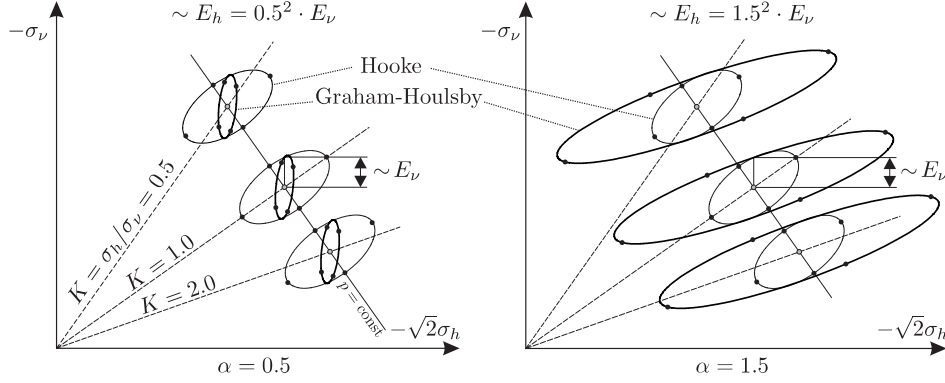
Figure 6. Response envelopes for linear isotropic Hooke's model and linear cross-anisotropic Graham-Houlsby model; $\nu = \nu_{vh} = \nu^*/\alpha = 0.2$; the stiffness moduli are scaled for visualisation on both graphs with $E = E_v = E^*$

et al. [19], Niemunis and Cudny [20]). The sound non-linear hyperelastic model that avoids these problems may be derived from the elastic potential, which is a scalar function of stress $W(\boldsymbol{\sigma})$ or strain $W(\boldsymbol{\varepsilon})$. In the case of function $W(\boldsymbol{\sigma})$, the hyperelastic compliance $\boldsymbol{C}^e$ is obtained by the following differentiation:

$$C^e_{ijkl} = \frac{\partial^2 W(\boldsymbol{\sigma})}{\partial \sigma_{ij} \partial \sigma_{kl}} \tag{22}$$

The stiffness is obtained from the inversion: $\boldsymbol{D}^e = (\boldsymbol{C}^e)^{-1}$.

Among the elastic potentials proposed in the literature, it is difficult to find functions based on typical parameters available to practising engineers. One of the interesting proposals is the function introduced by Vermeer [21]:

$$W(\boldsymbol{\sigma}) = \frac{3 p_{\text{ref}}^{1-\beta}}{2 G^{\text{ref}} (1+\beta)} \left(\frac{1}{3} \sigma_{ij} \sigma_{ij} \right)^{(1+\beta)/2} \tag{23}$$

where G^{ref} is the shear modulus at the reference pressure p_{ref} and β is a material constant. After differentiation, the compliance has the following form:

$$C^e_{ijkl} = \frac{1}{2G} \left[\delta_{ik} \delta_{jl} - (1-\beta) \frac{\sigma_{ij} \sigma_{kl}}{\sigma_{rs} \sigma_{rs}} \right] \tag{24}$$

with stress-dependent shear modulus

$$G = G^{\text{ref}} \left(\frac{\sqrt{\frac{1}{3} \sigma_{rs} \sigma_{rs}}}{p_{\text{ref}}} \right)^{1-\beta} \tag{25}$$

It is important for the implementation of the model that the compliance matrix may be inverted analytically and the final form of the stiffness matrix is:

$$D^e_{ijkl} = 2G \left[\delta_{ik} \delta_{jl} - \frac{(\beta-1)}{\beta} \frac{\sigma_{ij} \sigma_{kl}}{\sigma_{rs} \sigma_{rs}} \right] \tag{26}$$

The stiffness is a homogeneous function of stress of order $1-\beta$. The value of β must satisfy the condition $\beta \neq 0$. This limits the use of the model only to simulations

of dense granular soils or over-consolidated fine-grained soils. For lightly over-consolidated and normally consolidated fine-grained soils, the stiffness is changing as a linear function of stress with a proportionality constant, commonly known as the swelling index, which would imply the value of $\beta = 0$.

The stress dependency of Vermeer's hyperelastic stiffness is illustrated in Figure 7. The response envelopes for the hyperelastic model are confronted here with those for the linear isotropic elasticity. For the isotropic stress condition $p = p_{\text{ref}}$, the response envelopes for both models are the same, assuming the following relation between their parameters:

$$G^{\text{ref}} = \frac{E^{\text{ref}}}{2(1+\nu)} \tag{27}$$

$$\beta = -2 + \frac{3}{1+\nu} \tag{28}$$

where E^{ref} is the Young's modulus at the reference pressure $p = p_{\text{ref}}$.
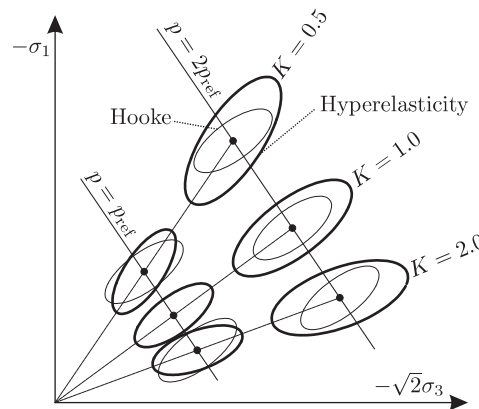

Figure 7. Response envelopes for linear isotropic Hooke's model and non-linear hyperelastic Vermeer's model; $\nu = 0.2$, $\beta = -2 + 3/(1+\nu) = 0.5$; the stiffness moduli are scaled for visualisation

The size of the response envelopes for the hyperelastic stiffness increases with the stress. Additionally, the envelopes are rotated for deviatoric stress states ($K \neq 1.0$) and oriented along the radial stress paths ($K = const$). This latter characteristic of the stiffness is termed stress-induced anisotropy.

3.4. Non-linear para-elastic stiffness

In the previous subsections, the stiffness is formulated within the theory of elasticity for the stress states limited by the conventional yield criterion. A simplification of this method is based on the assumption that soil layers in the given practical problem undergo almost exclusively small shear strains ($\gamma < 10^{-4}$). However, for intermediate strains (10^{-4} to 10^{-3}), dissipation of energy is observed and in the case of cyclic loading, the stress-strain curves become hysteretic. For a monotonic loading, the stiffness gradually decreases with the accumulated shear

strain. This phenomenon is ascribed to the small-scale local yielding and fretting at the interparticle contacts. Such a behaviour may be described in the simple shear case by the hyperbolic equation (Hardin and Drnevich [22]):

$$\frac{G^s}{G_0} = \frac{1}{1 + |\gamma/\gamma_r|} \tag{29}$$

where G^s is the actual secant shear modulus, G_0 is the shear modulus at very small strains and $\gamma_r = \tau_{failure}/G_0$ is the threshold shear strain. The strain history is represented here only by a single component of the shear strain. For general cases, the shear strain invariant may be used:

$$\gamma = \frac{3}{2}\varepsilon_q = \sqrt{\frac{3}{2}e_{ij}e_{ij}} \tag{30}$$

where e is the strain deviator ($e_{ij} = \varepsilon_{ij} - \frac{1}{3}\varepsilon_{kk}\delta_{ij}$).

Within simple elastic-ideally plastic models, which are used regularly in practice, the fact that the stiffness decays with the accumulation of shear strains is provided for by using constant secant stiffness moduli for the expected strains, rather than small strain. However, this procedure may be erroneous as the intensity of stiffness reduction relates to the loading direction and the stiffness increases suddenly for sharp stress path reversals (Richardson [23]). In constitutive modelling, these phenomena are possible to simulate only by a careful tracing of the stress-strain history. Typically, additional yield surfaces are introduced in the stress space to control and record changes of the stress path (Mróz [24], Al-Tabbaa and Muir Wood [25], Stallebrass [26]). Other original proposals are formulated by Simpson [27], where the loading history is captured solely in the strain space and by Niemunis and Herle [28], where the so-called *intergranular strain* is introduced, which is an additional tensorial state variable within the hypoplastic model. These modelling methods aspire to being complete solutions which cover all known features of the constitutive behaviour. However, their use in routine design is rather uncommon and requires material parameter sets, which are still far from being standardised.

In this study, a simple approach based on the well-known empirical formula (29) is applied. The shear strain history will be controlled only by a scalar variable and hence the application of the resulting model will be limited to the monotonic loading cases. The stiffness decay of the shear modulus is introduced into the hyperelastic stiffness (26). The resulting stiffness is no longer conservative and cannot be called hyperelastic. It may be classified as a para-elastic model where thermodynamic considerations are abandoned.

A modification of the Hardin-Drnevich hyperbolic equation proposed by Santos and Correia [29] is used:

$$\frac{G^s}{G_0} = \frac{1}{1 + \frac{3}{7}\gamma/\gamma_{0.7}} \tag{31}$$

where $\gamma_{0.7}$ is the threshold shear strain, for which the secant shear modulus G^s drops to a value of $0.7G_0$. This equation is shown to give satisfactory results and it

is implemented by Benz [30] into the new constitutive model within a commercial finite element code. For the incremental loading in the numerical calculations, the tangent shear modulus G^t is needed:

$$\frac{G^t}{G_0} = \left(\frac{\gamma_{0.7}}{\gamma_{0.7} + \frac{3}{7}\gamma}\right)^2 \tag{32}$$

After reaching a certain value of accumulated shear strain, the tangent modulus is reduced to a very low value. However, for larger shear strains, the strength criterion is reached and elasto-plastic stiffness is applied in the model. Therefore, it is better to specify the minimum value for the tangent shear modulus inside the yield surface $G^t = G^t_{\min}$. In the model formulated by Benz [30], the minimal tangent shear modulus is equal to the secant unloading-reloading shear modulus. This cutting-off of the stiffness degradation curve is performed for the shear strain γ_{co}, which may be calculated from the following equation:

$$\gamma_{co} = \frac{7}{3}\left(\sqrt{\frac{G_0}{G^t_{\min}}} - 1\right)\gamma_{0.7} \tag{33}$$

The shape of the stiffness degradation curves for tangent and secant moduli are shown in Figure 8, where the threshold strains used in the para-elastic model have also been indicated.
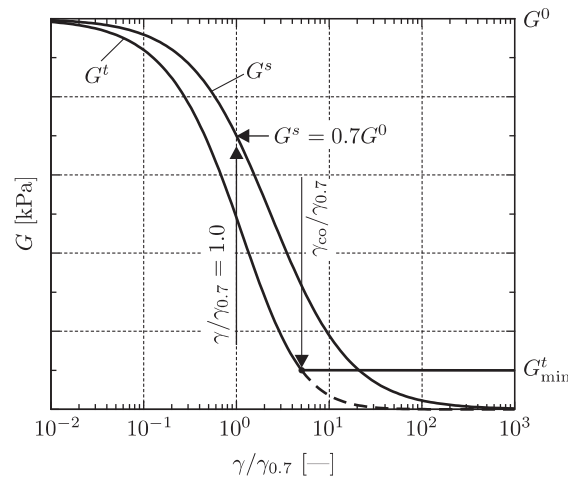

Figure 8. Stiffness reduction curves used in the para-elastic model. The decay of secant (G^s) and tangent (G^t) shear moduli as well as the effect of the threshold parameters $\gamma_{0.7}$, γ_{co} are shown

The threshold strain $\gamma_{0.7}$ is assumed to be constant and it does not depend on the current stress level. Therefore, the stiffness decay is applied to the reference shear modulus G^{ref} in the Equation (25), according to:

$$G^{\mathrm{ref}} = G_0\left(\frac{\gamma_{0.7}}{\gamma_{0.7} + \frac{3}{7}\gamma}\right)^2 \tag{34}$$

Note that the small strain modulus G_0 is also stress-dependent and should be estimated at the reference mean pressure p_{ref}.

During the implementation of the algorithm of small strain models, it is very important to apply a substepping scheme, since generally large strain increments can be delivered from the main program to the stress integration procedure. Small increments of loading are needed to avoid overshooting the non-linear stiffness changes in the small strain region. In the calculations presented in this article, the substepping is applied for the strain increments, the norm of which ($\|\Delta\boldsymbol{\varepsilon}\| = \sqrt{\Delta\varepsilon_{ij}\Delta\varepsilon_{ij}}$) is larger than 10^{-5}.

4. Calculations

The calculations of the boundary problem of the excavation-induced deformation are performed with the finite element method. The geometry and discretisation of the analysed plane strain model are shown in Figure 2. The triangular 6-node $\boldsymbol{u}-p$ quadratic elements are used in the calculations, in order to allow coupled analysis of the soil skeleton deformation and varying pore-water pressure. All calculation phases are executed using the updated mesh option, and consolidation of all soil layers is allowed during the numerical simulation of the excavation, *i.e.* dissipation and build-up of the excess pore-water pressure is possible in the same time increment, within the analysed area. An unstructured finite element mesh is applied with local refinement in the vicinity of structural members, where some stress concentrations can be expected. No regularisation method is applied as the back-analysed boundary problem concerns the pre-failure soil behaviour. However, because no strain-softening is involved within material models, an application of different meshes would produce some slight differences in the results.

All structural elements of the diaphragm walls and slabs are modelled with continuum finite elements and linear elastic material characteristics ($E = 3 \cdot 10^7 \, \text{kPa}$, $\nu = 0.1$). The floor slab is simulated by a single horizontal spring element with axial stiffness $EA = 1.1 \cdot 10^5 \, \text{kN/m}$.

The extent of the boundary problem is chosen so as to minimise the side effects on the deformation. Sliding boundaries are used on the sides of the model, whereas fixed boundaries are applied at the bottom. In the initial analysis, the interaction between the slurry walls and soil was modelled alternatively with or without interface elements. The observed deformation was not influenced by this exchange and the mobilised wall friction angle was low. The final results are shown for tied interfaces with local mesh refinement, both for the slurry walls and slab, where direct sliding is further reduced by the blinding concrete interlayer.

The initial stress distribution is applied according to the K_0 values given in Figure 3. These values are obtained from dilatometric tests. In the first phase of the calculation, the neighbouring bank building is introduced to the model. In the next phase, the diaphragm walls are introduced by changing the material model from a soil model to the linear elastic model, characteristic of the concrete in the area reserved for the diaphragm walls. After this phase, all strain history

and displacements are reset to zero. The subsequent simulation phases concern the gradual execution of the excavation with the installation of the floor slab, according to the documented time schedule. The bottom of the excavation was reached after 200 days. Reloading phases related to the slab-making and finalising of the underground part of the building were completed within the next 35 days.

4.1. Parameters of the material models

Material parameters listed in Figure 3 are obtained from standard *in situ* surveys and laboratory tests on undisturbed samples. They are commonly used in the Mohr-Coulomb model for the numerical simulations of soil-structure interaction problems in similar local, geological conditions. The elastic moduli in this record represent the secant stiffness of soils for typical geotechnical operations.

The parameters used in the linear anisotropic Graham-Houlsby model are listed in Table 1. In the analysis, three values of the parameter α are examined. For $\alpha = 1.0$, the model reproduces the isotropic Hooke's stiffness and for $\alpha = 1.25$ and $\alpha = 1.35$, the obtained anisotropic stiffness represents the behaviour of the over-consolidated soils, where horizontal stiffness is higher than the vertical one. For $\alpha > 1.0$, the parameters E^* and ν^* are adjusted in such a way that the sizes of the main axes of the response envelope are constant for different values of α. In so doing, the parameter α controls only the rotation of the anisotropic response envelopes relative to the orientation of the response envelope for isotropic stiffness ($\alpha = 1.0$). The same degree of anisotropy is assumed for all natural soil layers.

Table 1. Stiffness parameters used in the linear anisotropic Graham-Houlsby model

| layer | $\alpha = 1.0$ | | $\alpha = 1.25$ | | $\alpha = 1.35$ | |
	$\nu^* = \nu$ [—]	$E^* = E$ [kPa]	ν^* [—]	E^* [kPa]	ν^* [—]	E^* [kPa]
1	0.30	35 660	—	—	—	—
2	0.20	43 200	0.25	25 620	0.27	20 750
3	0.20	37 350	0.25	22 150	0.27	17 940
4	0.15	104 180	0.19	65 440	0.18	71 810
5	0.15	84 290	0.19	52 940	0.20	44 140
6	0.10	163 290	0.13	105 820	0.14	89 600

In this study, the behaviour of the shallow fill (layer 1) is simulated with the isotropic linear stiffness inside the yield locus in all calculations.

The parameters used in the non-linear hyperelastic model are listed in Table 2. The reference shear modulus $G^{\rm ref}$ and the exponent β are calculated from the basic stiffness parameters shown in Figure 3, using relations (27) and (28). The response of this model is compared for three different values of the reference pressure $p_{\rm ref}$, which are not routinely specified.

In the non-linear para-elastic model with stiffness degradation, the parameters obtained from the seismic tests are used. They are listed in Table 3. The small strain shear moduli G_0 are related to the operational Young's moduli values shown in Figure 4. The values of the Poisson's ratios and exponents β are

Table 2. Stiffness parameters used in the non-linear hyperelastic model

layer	G^{ref} [kPa]	ν [—]	β [—]	p_{ref} [kPa]
2	18 000	0.20	0.50	100/250/400
3	15 560	0.20	0.50	100/250/400
4	45 290	0.15	0.61	100/250/400
5	36 650	0.15	0.61	100/250/400
6	74 220	0.10	0.73	100/250/400

the same as in the calculations with the hyperelastic model. The minimal tangent shear modulus is simply chosen relative to the small strain shear modulus as $G^t_{\text{min}} = G_0/5$. The threshold shear strain $\gamma_{0.7}$ and the reference pressure p_{ref} are assumed constant for all natural soil layers.

Table 3. Stiffness parameters used in the non-linear para-elastic model

layer	G_0 [kPa]	G_{min} [kPa]	$\gamma_{0.7}$ [—]	p_{ref} [kPa]
2	54 170	10 834	0.0001	100
3	30 000	6 000	0.0001	100
4	146 090	29 218	0.0001	100
5	146 090	29 218	0.0001	100
6	92 730	18 546	0.0001	100

4.2. Simulation results

The excavation-induced deformation of the surrounding ground is the main focus of the simulations. Due to the over-consolidation, the soil layers exhibit good strength properties and no significant yielding within the numerical model is noticed. Some passive yielding is observed at the bottom of the excavation and in the area of the diaphragm wall embedment. Generally, from the field measurements of the analysed excavation case, as well as from the observations of similar excavations in the same geological area, high swelling is evidenced with maximal magnitudes located in the bottom centre. The displacement of the excavation bottom is difficult to measure, however, it is reported to have reached a heave of several centimetres. In the simulations, the heave of the excavation bottom is the highest for the anisotropic model (0.058m for $\alpha = 1.35$) and for the para-elastic model (0.056m). Lower values are obtained for the hyperelastic model (0.025m for $p_{\text{ref}} = 400$kPa).

A precise comparison is presented for the monitored points of the bank building foundation and the diaphragm wall at the height of the floor slab. The time-displacement curves are shown in Figures 9–11 for anisotropic, hyperelastic and para-elastic stiffness formulations, respectively.

The time progression of the heave observed at point A is most accurately reproduced in the simulations with para-elastic stiffness. For linear anisotropic stiffness, the best results are obtained for high values of the parameter α,
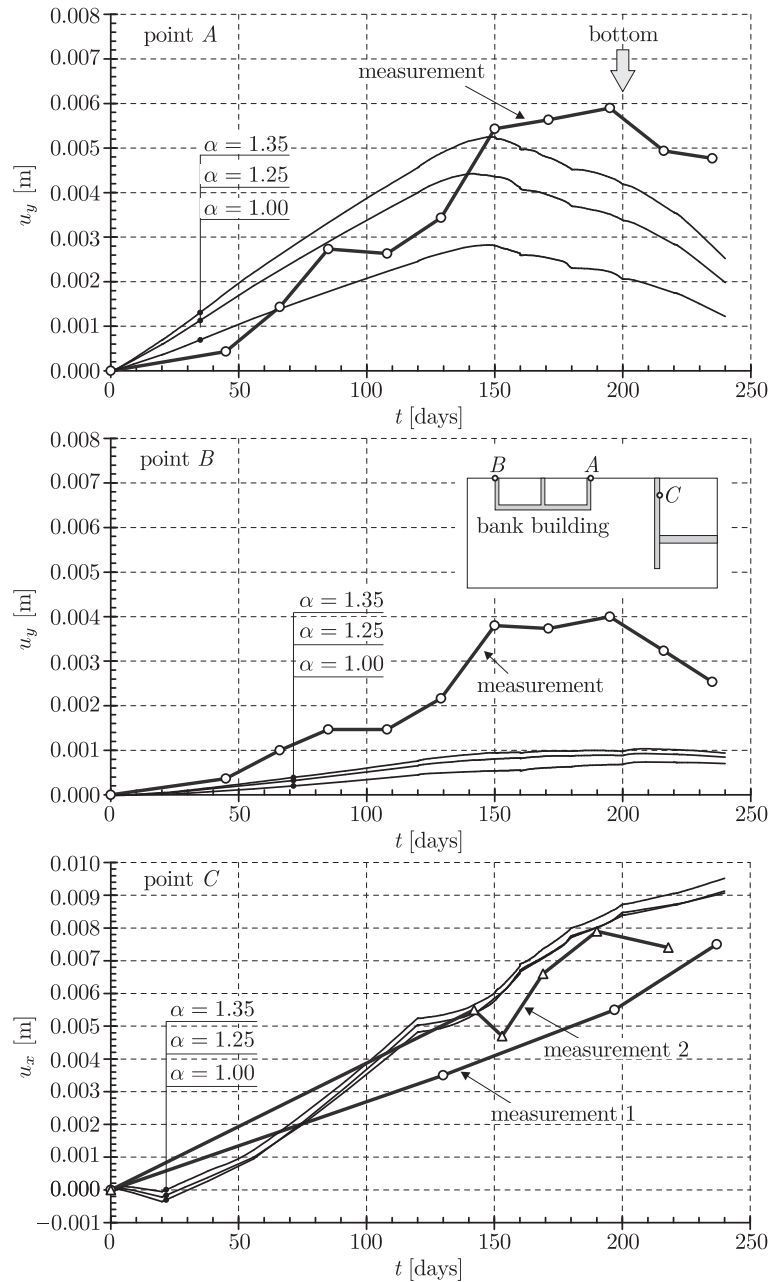
Figure 9. Time-displacement curves from simulations with the linear anisotropic stiffness for different values of the parameter α
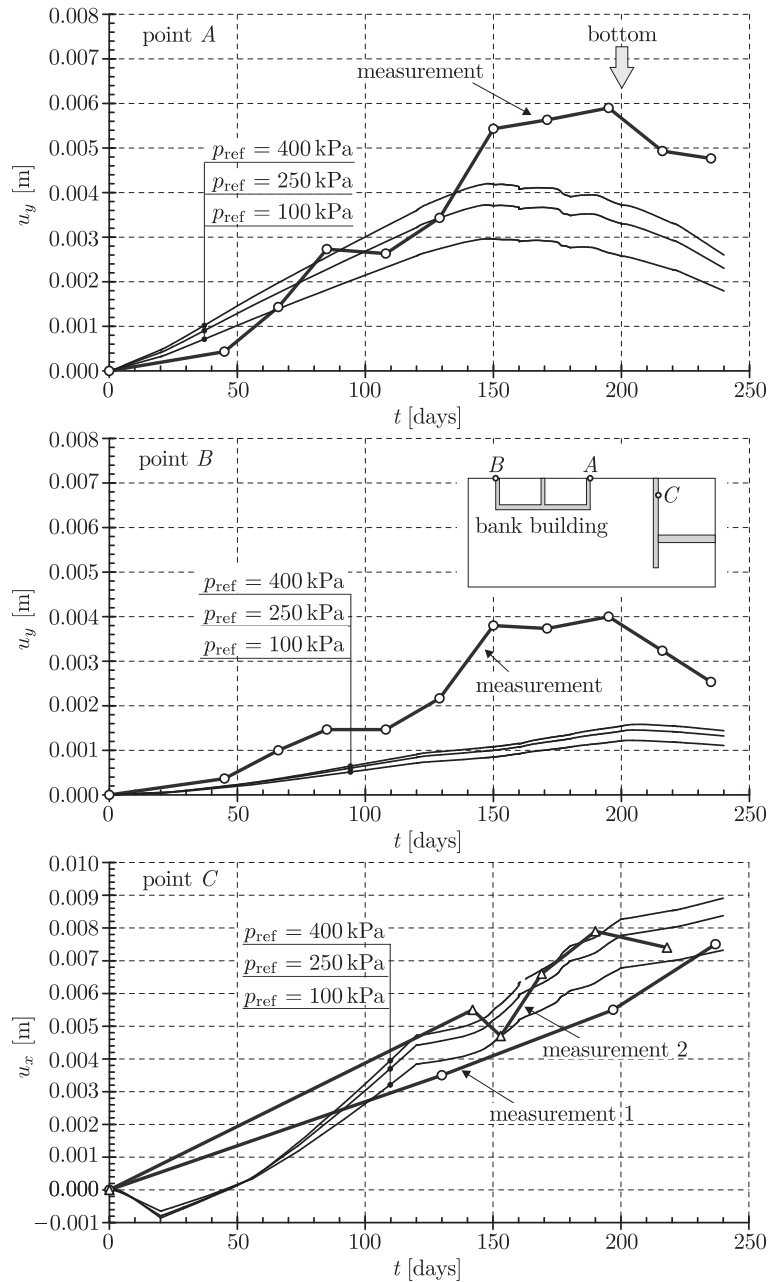
Figure 10. Time-displacement curves from simulations with the non-linear hyperelastic stiffness for different values of the reference pressure p_{ref}
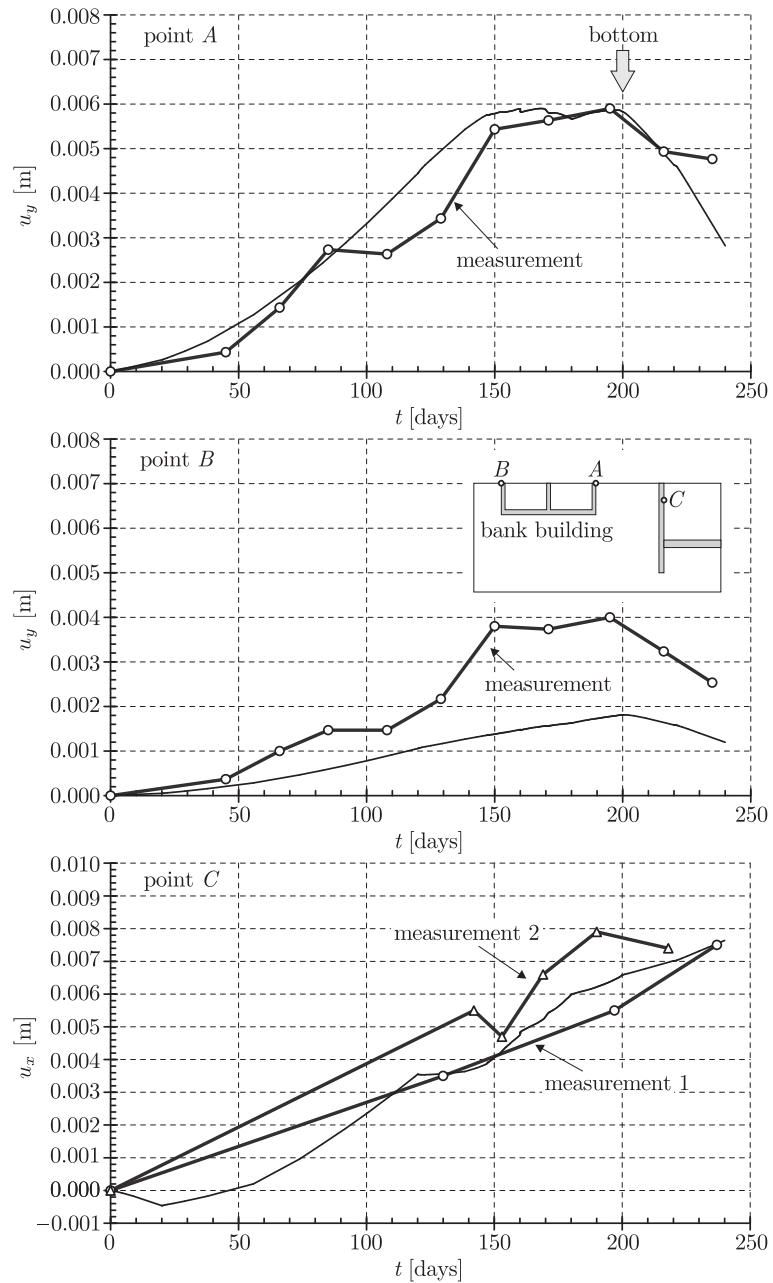
Figure 11. Time-displacement curves from simulations with the para-elastic stiffness

representing the anisotropy ratio, however, the calculated progression differs from the measured one. Due to the constant average stiffness in this model, calculated displacements are higher at the initial phase of the excavation. It is also important to note that the peak value of the heave occurs long before reaching the bottom of the excavation and the subsequent reloading phase. The shape of the time-displacement curve is better reproduced when using the hyperelastic stiffness. Nevertheless, the calculated heave is underestimated here.

A similar discrepancy between the calculated and measured displacements is observed for point B, located at the back of the bank building. Here, the relative differences are greater and, generally, the heave obtained from all simulations is underestimated. The results of simulations with the para-elastic stiffness are in better accordance with observations. These inaccuracies of the simulations may be attributed to the simplified numerical model of the bank building foundation.

The calculated and measured horizontal displacements of the diaphragm wall (point C) are in good agreement for all applied material characteristics. In Figures 9–11 two independent measurement results of this displacement are shown. It should be remarked that the imposed initial value of the K_0 coefficient and the axial stiffness of the floor slab, which is difficult to estimate precisely, significantly influence the calculated horizontal displacement of the wall.

The calculated changes of the surface vertical displacements are shown in Figure 12 for the para-elastic model, which yielded the best fit to the monitored behaviour at points A, B and C. The distribution of the incremental displacement
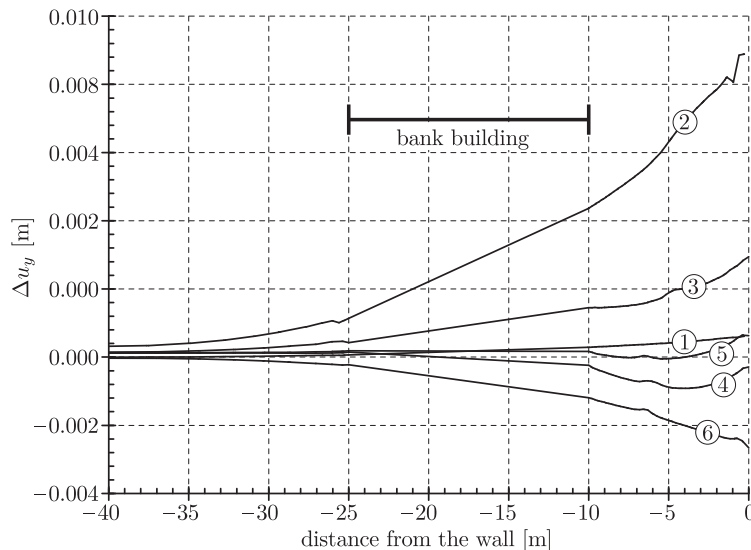

Figure 12. Surface incremental displacements Δu_y at different excavation phases from simulations with the para-elastic stiffness: (1) 1.0m excavation, 20 days; (2) 5.0m excavation with installation of the floor-slab, 100 days; (3) 1.8m excavation, 40 days; (4) 1.2m excavation, 20 days; (5) 1.2m excavation, 20 days; (6) installation of the base slab and reloading, 40 days

Δu_y is shown for the successive phases of the excavation. Initially, the ground surface displayed a decrease in the heave with the distance from the diaphragm wall. When the excavation depth of 7.8 m was reached, the area between the bank building and the excavation started to settle, forming the distinctive trough. However, the sum of the vertical displacements remained positive, even for the final excavation depth before concreting the slab.

5. Conclusions

An example case of excavation is analysed by means of a FEM simulation. Nowadays, this modelling technique is becoming favoured and is often used in routine design. The main focus of the article was to validate calculations with different constitutive models by comparing them with results of field monitoring. For the chosen geometry and discretisation of the boundary problem, four stiffness formulations were examined by comparing the calculated and measured displacements. The applied elasto-plastic models were simple and the choice of the material parameters was based on the documentation typically available in practice, with the exception of small strain characteristics, which were estimated here from seismic tests.

The influence of the anisotropy is significant and it was shown that for parameters representing high inherent anisotropy of the over-consolidated deposits, the results are closer to the measurements, however, the predicted progression of the ground deformation differs from the observed one. The general consequence of increasing the anisotropy factor on the results of an excavation simulation is a larger heave of the surrounding ground, and the occurrence of larger differences along the monitored distance. Introducing the non-linear stress dependency of the stiffness in the hyperelastic model with stress induced anisotropy did not improve the predictions significantly and the observed high heave of the neighbouring building is still simulated on the lower level. The best results are obtained for the para-elastic formulation, where the stress dependency of the stiffness is coupled with the degradation of the reference shear modulus with the accumulated shear strain. An extension of such a model presented in the article is very simple and limited to the monotonic loading or reloading.

It was demonstrated that taking into account the anisotropy and stress, as well as strain dependency of the stiffness, in the pre-failure behaviour of over-consolidated soils is important for realistically estimating deformation. However, standard soil parameters available for geotechnical engineers are not sufficient for this task. Additional testing should require the estimation of the small strain stiffness moduli, preferably by *in situ* or laboratory seismic methods. The stress dependency and anisotropy factor can be estimated from known empirical formulas or, in the case of important geotechnical structures, by extended laboratory testing. For monotonic loading, small strain tangent stiffness and intermediate secant stiffness need to be incorporated within the constitutive model, as was exemplified in the article.

References

[1] Matsuoka H and Nakai T 1977 *Proc. 9th Int. Conf. Soil Mech. and Found. Eng. Spec. Session* (Murayama and Schofield, Eds), Tokyo, **9**, pp. 153–162

[2] Barański M, Szczepański T, Popielski P and Dąbska A 2008 *Dev. Urban Areas and Geotech. Eng.*, Saint Petersburg, Russia, pp. 173–179

[3] Matthews M C, Hope V S and Clayton C R I 1996 *Proc. ICE, Geotech. Eng.* **119** 84

[4] Eekelen H A M 1980 *Int. J. Num. and Anal. Meth. Geomech.* **4** 89

[5] Brinkgreve R B J, Broere W and Waterman D 2006 *Plaxis Finite Element Code for Soil and Rock Analyses*, Version 8

[6] Jeremić B and Sture S 1997 *Mech. Cohesive-frictional Materials* **2** 165

[7] Jovičić V and Coop M R 1998 *Geotech. Testing J.* **21** (1) 3

[8] Poulos H G 1972 *J. Soil Mech. and Found. Div.* **98** (SM8) 843

[9] Simpson B, Atkinson J H and Jovičić V 1996 *The Influence of Anisotropy on Calculations of Ground Settlements above Tunnels, Geotechnical Aspects of Underground Construction in Soft Ground* (Mair and Taylor, Eds), Balkema, Rotterdam, pp. 591–594

[10] Addenbrooke T I, Potts D M and Puzrin A M 1997 *Géotechnique* **47** (3) 693

[11] Kung G T C, Hsiao E C L and Juang C H 2007 *Canadian Geotech. J.* **44** 726

[12] Pickering D J 1970 *Géotechnique* **20** (2) 217

[13] Lings M L, Pennington D S and Nash D F T 2000 *Géotechnique* **50** (2) 109

[14] Graham J and Houlsby G T 1983 *Géotechnique* **33** (2) 165

[15] Gudehus G 1979 *Proc. 3rd Int. Conf. Num. Meth. Geomech.*, Balkema, Aachen, pp. 1309–1323

[16] Ohde J 1936 *Der Bauingenieur* **20** 451

[17] Janbu N 1963 *Proc. 3rd European Conf. Soil Mech. and Foundation Eng.*, Wiesbaden, pp. 19–25

[18] Houlsby G T and Wroth C P 1991 *Soils and Found.* **31** (3) 138

[19] Zytynski M, Randolph M F, Nova R and Wroth C P 1978 *Int. J. Num. and Anal. Meth. Geomech.* **2** 87

[20] Niemunis A and Cudny M 1998 *Comp. and Geotech.* **23** 221

[21] Vermeer P A 1985 *A Five Constant Model Unifying well Established Concepts, Constitutive Relations of Soils* (Gudehus, Darve and Vardoulakis, Eds), Balkema, Rotterdam, pp. 175–197

[22] Hardin B O and Drnevich V P 1972 *J. Soil Mech. and Found. Div.*, ASCE, **98** (SM7) 667

[23] Richardson D 1988 *Investigations of Treshold Effects in Soil Deformations*, PhD Thesis, City University, London

[24] Mróz Z 1967 *J. Mech. and Physics of Solids* **15** 163

[25] Al-Tabbaa A and Muir Wood D 1989 *An Experimentally Based Bubble Model for Clay, Numerical Models in Geomechanics* (Pande and Pietruszczak, Eds), Elsevier Applied Science, London, **III**, pp. 91–99

[26] Stallebrass S E 1990 *Modelling the Effect of Recent Stress History on the Deformation of Overconsolidated Soils*, PhD Thesis, City University, London

[27] Simpson B 1992 *Géotechnique* **42** (4) 541

[28] Niemunis A and Herle I 1997 *Mech. Cohesive-frictional Materials* **2** (4) 279

[29] Santos J A and Correia A G 2001 *Proc. 15th Int. Conf. Soil Mech. and Geotech. Eng.*, Istanbul, Turkey, **1**, pp. 267–270

[30] Benz T 2007 *Small-strain Stiffness of Soils and its Numerical Consequences*, PhD Thesis, University of Stuttgart